Journal of The Electrochemical Society, **155** (10) B1066-B1076 (2008)
0013-4651/2008/155(10)/B1066/11/$23.00 © The Electrochemical Society

Modeling the Dynamic Water Transport in the Porous Layers of PEM Fuel Cells Based on Numerical Upscaling

Julia Hermann[a] **and Christoph Ziegler**[b,z]

[a]*Fraunhofer Institute for Solar Energy Systems, 79110 Freiburg, Germany*
[b]*University of Freiburg, 79110 Freiburg, Germany*

A one-dimensional two-phase model is developed to study the dynamic water transport in the porous layers of polymer electrolyte membrane (PEM) fuel cells. Liquid water transport and diffusion of oxygen are described by a coupled differential equation system. Capillary pressure, relative permeability, and oxygen diffusivity are determined based on the results of microstructural simulations. The model is compared quantitatively to two different chronoamperometric experiments, potential step voltammetry, and sine wave testing, whereby the optimization algorithm of Nelder and Mead is used. The model predicts the measured dynamic current behavior for both experiments. As a result of the optimization, important two-phase and material parameters are extracted.
 [DOI: 10.1149/1.2957487]

Manuscript submitted February 27, 2008; revised manuscript received June 17, 2008. Published August 25, 2008.

The fuel cell is attracting increasing attention as an important energy converter, because it is quiet, nonpolluting, and energy efficient. Polymer electrolyte membrane (PEM) fuel cells use hydrogen and air to convert chemical energy directly into electricity, producing only water and heat as by-products. The oxygen reduction reaction (ORR) takes place in the catalyst layer of the cathode. Protons resulting from the hydrogen oxidation reaction in the anode migrate through the membrane to the cathode and react with oxygen to produce water and heat. A porous gas diffusion layer (GDL) is located on each electrode between the flow field and catalyst layer to distribute the reactants evenly.

The optimization of fuel cells requires a broad understanding of the underlying physical processes. Currently, a significant limitation of the fuel cell performance at high current densities originates in the blockage of the pores of the GDL by liquid water, which constrains the reactant transport to the catalyst layers. This process is known as mass transport limitation. Modeling the two-phase transport in the porous layers of PEM fuel cells provides a basis for understanding this process and makes systematic material design possible. A crucial task related to the two-phase modeling is the parametrization of saturation-dependent quantities such as capillary pressure and relative permeability of liquid water.

Various approaches exist to describe the liquid water transport and mass transport limitation phenomena in the porous layers of PEM fuel cells. A detailed discussion of fundamental fuel cell models including works on transient phenomena prior to 2004 can be found in Ref. 1. Pasaogullari and Wang[2] derived a one-dimensional analytical solution for the liquid water transport across the GDL in both hydrophobic and hydrophilic gas diffusion media by using the gradient of the capillary pressure. In addition, they studied the influence of the GDL wettability on the liquid water transport in detail. In Ref. 3, Pasaogullari and Wang evaluated the degree of approximation of the unsaturated flow theory (UFT) by using the multiphase mixture model. In UFT, a constant gas pressure is assumed, and the capillary pressure gradient corresponds to the negative liquid water pressure gradient. Nam and Kaviany[4] published a one-dimensional model to describe the liquid water transport in the GDL and an adjacent microporous layer (MPL), using the UFT. They concluded that by creating a saturation step at the interface between the GDL and MPL, the cell performance is improved. Wang et al.[5] developed a two-dimensional two-phase model of a PEM fuel cell. A threshold current density was defined corresponding to the first appearance of liquid water at the membrane–cathode interface. Hence, single-phase and two-phase regimes both exist in the cathode. In the two-phase model of Birgersson et al.,[6] where mass, heat, and charge transport are described for the complete PEM fuel cell, the simulation is carried out for two different expressions of the capillary pressure, one based on the Leverett function, and one defined by Natarajan and Nguyen.[7] The former one leads to a much higher liquid water saturation in the fuel cell, causing partial flooding in the active layer of the cathode. Birgersson et al. also carried out a scale analysis by nondimensionalizing the governing equations to determine the relative importance of various transport mechanisms. As one result, the convection of species in the cathode is negligible compared to the diffusion, when a flow field without induced forced flow is used. This corresponds to the UFT, where the gradient of the gas pressure is set to zero. In contrast to the publications named above, the two-phase models of Ref.[8-12] have been validated by comparing the simulation results to experimental data, given by steady-state polarization curves. You and Liu[8] investigated the threshold current density at which two-phase flow is formed and found that it depends on the characteristics of the gas diffusion material. In the two-phase cathode model of Rao et al.,[11] the relative permeability of liquid water and the derivative of the capillary pressure with respect to the liquid water saturation are regarded as constant. Acosta et al.[12] developed a two-dimensional two-phase model of the cathode, where the capillary pressure and the relative permeability of water were determined experimentally by using mercury intrusion porosimetry, assuming a hydrophobic GDL. However, deviations between simulation data and measured polarization curves at high fuel cell loads showed that a more detailed consideration of the partially hydrophilic behavior of the GDL is necessary.

The above-mentioned studies investigate only the cell steady-state behavior, while for many applications of fuel cells, such as in automobiles, their dynamic performance is important, given the rapid change of the operating conditions with time. Dynamic models describing the liquid water transport in the porous layers of PEM fuel cells have been published in Ref. 7 and 13-16. Ziegler et al.[13] developed a two-phase PEM fuel cell model, which was used to simulate cyclic voltammograms. In the one-dimensional cathode GDL model of Song et al.,[14] the time needed to reach steady-state water saturation was examined and plotted against various model parameters such as the contact angle of the GDL. The two-phase model of Meng[15] considered the effects of the liquid water transport on the dynamic response of a PEM fuel cell to a sudden change of the cell potential. It was found that under isothermal conditions, the presence of liquid water in the porous media increases the current overshot and undershot. Wang and Wang[16] considered the fuel cell dynamics under both fully humidified and underhumidified conditions using a three-dimensional model. They found that in underhumidified situations there is simultaneous presence of a single-phase region and a two-phase zone, whereas the interface between the two is a moving boundary. Natarajan and Nguyen[7] determined that the performance of the cathode is highly dependent on the dynamics of the liquid water transport. Their simulation results showed that the liquid water transport is the slowest mass transfer and mainly responsible for the mass transport limitation phenomena. By fitting the two-phase model to experimental data, the capillary-saturation ex-

[z] E-mail: christoph.ziegler@imtek.uni-freiburg.de

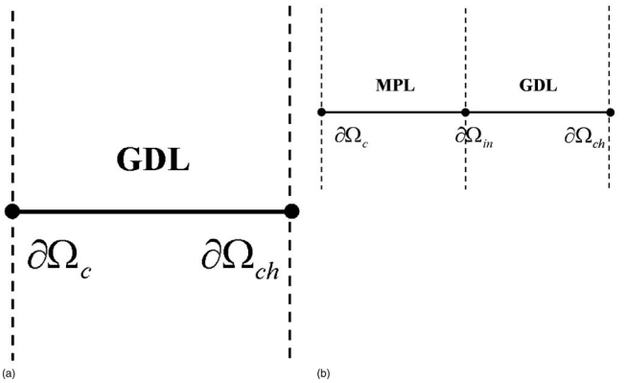

Figure 1. Geometrical configurations. (a) GDL, (b) GDL + MPL.

pression was obtained. The model was validated by comparing the simulation results to a measured steady-state polarization curve. However, because fuel cells cannot be operated at steady state without adjustment control in the two-phase regime, model validation with dynamic experimental data is necessary for transient models.

In all above-mentioned publications, except for Ref. 6, 7, and 11, the Leverett function, in a form suggested by Udell,[17] is used to describe the capillary pressure–saturation relationship. For the relative permeability, an expression due to Wang[18] is used in all publications except for Ref. 7, 11, and 12. Both the Leverett and Wang expressions are empirical correlations obtained by investigations on soil tests. As the structure of the porous layers in PEM fuel cells is different from that of soil tests, it is a crucial task to adapt these empirical expressions for application to PEM fuel cells.

In this paper, a one-dimensional dynamic model of the porous transport layers of a PEM fuel cell at the cathode side is developed. Liquid water transport and oxygen diffusion are described by a partial differential equation system. Due to the coupling of the two transport mechanisms, mass-transport limitation phenomena occurring at high current densities can be expressed by the model. Capillary pressure, relative permeability, and oxygen diffusivity are determined by analyzing microstructural simulation data obtained by Becker et al.[19] The ORR in the cathode catalyst layer is described by boundary conditions using Tafel kinetics. The model represents a simplified approach to the description of mass-transport limitation with the benefit that problems of simulation times and parameter identification are minimized. The model is compared quantitatively to chronoamperometric measurements. The optimization algorithm of Nelder and Mead is used to fit the simulation results to the experimental data and extract model parameters.

Modeling and Simulation

Model equations.— Figure 1 shows the two one-dimensional geometrical configurations for which the model is solved. Figure 1a is the configuration across the GDL on the cathode side, Fig. 1b across a combination of GDL and MPL. The boundary $\partial\Omega_c$ describes the cathode side; $\partial\Omega_{\mathrm{ch}}$ is the boundary to the gas channels of the fuel cell. The boundary between GDL and MPL in Fig. 1b is denoted as $\partial\Omega_{\mathrm{in}}$.

The transport of liquid water in a porous medium is described by Eq. 1, using the liquid water saturation s_{l}

$$\pi_\kappa \rho_{\mathrm{l}} \frac{\partial s_{\mathrm{l}}}{\partial t} + \nabla \times (\rho_{\mathrm{l}} v_{\mathrm{l}}) = 0 \quad \text{with } \kappa = \mathrm{GDL,MPL} \qquad [1]$$

$$\mu_{\mathrm{l}} = -\frac{1}{\mu_{\mathrm{l}}} k_{\mathrm{rel,l}} K_{\mathrm{int},\kappa} \nabla p_{\mathrm{l}} \qquad [2]$$

In Eq. 1, no phase change of water is considered. ρ_{l}, μ_{l}, and p_{l} are the liquid water density, viscosity, and pressure. The saturation-dependent relative permeability of liquid water is termed $k_{\mathrm{rel,l}}$. The material properties of layer κ are given by the porosity π_κ and the intrinsic permeability $K_{\mathrm{int},\kappa}$. According to the UFT (see Ref. 3), the gradient of the gas pressure ∇p_{g} in the porous transport layers is set to zero. This yields for the gradient of the liquid water pressure

$$\nabla p_{\mathrm{l}} = \nabla p_{\mathrm{g}} - \nabla p_{\mathrm{c}} = -\nabla p_{\mathrm{c}} \qquad [3]$$

where p_{c} is the saturation-dependent capillary pressure.

The transport of oxygen is described by the Fickian diffusion equation

$$\pi_\kappa \rho_{\mathrm{O_2}} \frac{\partial y_{\mathrm{O_2}}}{\partial t} - \nabla \times (\rho_{\mathrm{O_2}} D_{\mathrm{O_2}} \nabla y_{\mathrm{O_2}}) = 0 \qquad [4]$$

where $y_{\mathrm{O_2}}$ and $\rho_{\mathrm{O_2}}$ are the volume fraction and the density of oxygen. $D_{\mathrm{O_2}}$ is the saturation-dependent diffusivity of oxygen.

For all simulations, the initial value of $y_{\mathrm{O_2}}$ is set to

$$y^0_{\mathrm{O_2}} = 0.21 \qquad [5]$$

The initial value of s_{l} is adjusted individually for each simulation to achieve good convergence. The respective values are given in the following sections.

If the GDL only is modeled (Fig. 1a), two boundary conditions for each of the variables s_{l} and $y_{\mathrm{O_2}}$ are needed. At the boundary to the gas channel, $\partial\Omega_{\mathrm{ch}}$, the water saturation s_{l} is set to zero (Eq. 6). For $y_{\mathrm{O_2}}$ the volume fraction of oxygen in dry air is used as a boundary condition (Eq. 7). This corresponds to the experimental condition of dry air supplied to the cathode side of the fuel cell[20]

$$s_{\mathrm{l}} = 0 \quad \text{at } \partial\Omega_{\mathrm{ch}} \qquad [6]$$

$$y_{\mathrm{O_2}} = 0.21 \text{ at } \partial\Omega_{\mathrm{ch}} \qquad [7]$$

The boundary conditions at $\partial\Omega_{\mathrm{c}}$ depend on the current density j_{c}

$$\frac{M_{\mathrm{l}}}{2F} \times j_c = N_{\mathrm{l}} \qquad [8]$$

$$-\frac{M_{\mathrm{O_2}}}{4F} \times j_{\mathrm{c}} = N_{\mathrm{O_2}} \qquad [9]$$

where N_{l}, $N_{\mathrm{O_2}}$ are the surface normal components of water and oxygen mass flux; M_{l}, $M_{\mathrm{O_2}}$ are the molar masses of water and oxygen, and F is the Faraday constant. The mass fluxes N_{l} and $N_{\mathrm{O_2}}$ are given by

$$N_{\mathrm{l}} = \frac{\rho_{\mathrm{l}}}{\mu_{\mathrm{l}}} k_{\mathrm{rel,l}} K_\kappa \nabla p_{\mathrm{l}} \qquad [10]$$

$$N_{\mathrm{O_2}} = \rho_{\mathrm{O_2}} D_{\mathrm{O_2}} \nabla y_{\mathrm{O_2}} \qquad [11]$$

The cathode current density j_{c} is described by the Tafel equation

$$j_{\mathrm{c}} = -d_{\mathrm{c}}(1 - s_{\mathrm{l}})^\beta a j_0 y_{\mathrm{O_2}} \exp\left(\frac{-\alpha z F n_{\mathrm{c}}}{RT}\right) \qquad [12]$$

where d_{c} is the thickness of the cathode layer. To account for the porous structure of the cathode layer, the active area per volume, denoted a, is introduced. Due to flooding processes, the active area on the cathode is reduced as the water saturation s_{l} increases; this is described by the term $(1 - s_{\mathrm{l}})^\beta$. The current density is further dependent on the volume fraction of oxygen $y_{\mathrm{O_2}}$. j_0, α, and z are, respectively, the exchange current density at the cathode, the asymmetry factor, and the number of electrons involved in the production of one water molecule. Experimental investigations[21-23] reveal a doubling of the Tafel slope $RT/(\alpha z F)$ for voltage values below 0.8 V that are relevant for the description of mass-transport limitation. The doubling of the Tafel slope corresponds to a change of z from 2 to 1, if the other parameters are held constant. A possible explanation of this phenomen, given by Parthasarathy et al.,[24] is a

change of the reaction mechanism. Based on this, we use

$$z = 1 \quad [13]$$

The cathode overpotential is termed η_c and is the sum of the activation overpotential $\eta_{A,c}$ and the concentration overpotential $\eta_{conc,c}$ at the cathode

$$\eta_c = \eta_{A,c} + \eta_{conc,c} \quad [14]$$

Ohmic losses due to the resistance of the membrane as well as the anode overpotential are not considered in the model. However, the use of a reference fuel cell in the experimental setup allowed separation of the anodic, cathodic, and ohmic overpotentials. Thus, an effective voltage U_{eff} could be determined by subtracting the anodic and the ohmic overpotentials from the cell voltage U_{cell}. Further on, an analytical function was fitted to U_{eff}, yielding the voltage U_{sim} which was used for simulation (see the Model Validation section for a detailed description of the determination of U_{sim}). The cathode overpotential η_c can hence be expressed by

$$\eta_c = U_{sim} - U_{oc} \quad [15]$$

where U_{oc} is the measured open-circuit voltage of the test cell.

If both GDL and MPL are modeled (Fig. 1b), an interface condition at $\partial\Omega_{in}$ is needed. Here, the continuity of the capillary pressure is required

$$p_{c,GDL} = p_{c,MPL} \text{ at } \partial\Omega_{in} \quad [16]$$

Because the gas pressure p_g is constant, this yields

$$p_{l,GDL} = p_{l,MPL} \text{ at } \partial\Omega_{in} \quad [17]$$

The model is solved using the simulation software Comsol. The partial differential equations are discretized using the finite element method. Because they are strongly nonlinear due to the nonlinearity of the saturation-dependent parameters, an implicit solver based on the Newton method is used.

Determination of saturation-dependent parameters.— To determine the saturation-dependent parameters, several empirical correlations for capillary pressure p_c and relative permeability $k_{rel,l}$ as well as an expression for the diffusivity of oxygen D_{O_2} have been fitted to datasets obtained by Becker et al.[19] from microstructural simulation using the pore morphology method. The best matching expressions were applied to Eq. 1–4. Starting from a three-dimensional (3D) tomography image of a Freudenberg GDL, Becker et al. created a 3D model of the GDL. For an arbitrary contact angle, the liquid water saturation was calculated for several capillary pressure values. Based on these results, other saturation-dependent parameters such as relative permeability, diffusivity, and thermal conductivity were determined.

Three empirical relations were found for the capillary pressure. They trace back to Leverett (especially in the form proposed by Udell[17]), Brooks-Corey,[25] and Van Genuchten.[26] The capillary pressure defined by Leverett and Udell is given by

$$p_c(s_l) = \sigma_l \cos\theta \sqrt{\frac{\pi}{K_{int}}} J(s_l) \quad [18]$$

where σ_l is the surface tension of liquid water at the phase boundary to air, and $\cos\theta$ is the contact angle of the medium. $J(s_l)$ is the Leverett function

$$J(s_l) = a s_l - b s_l^2 + c s_l^3 \quad [19]$$

with

$$a = 1.417$$

$$b = 2.120$$

$$c = 1.263$$

Brooks-Corey proposed the following expression for the capillary pressure

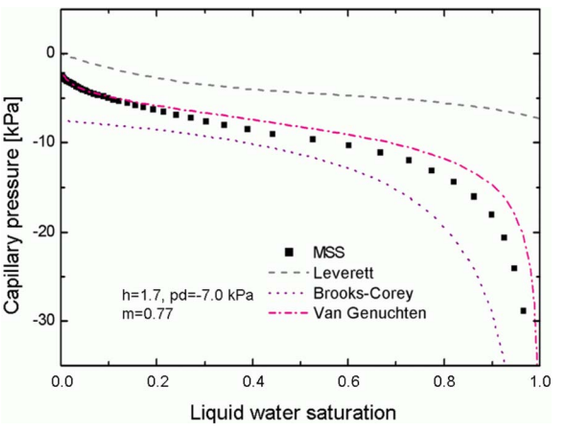

Figure 2. (Color online) Capillary pressure–saturation relation according to Leverett, Brooks-Corey, Van Genuchten, and microstructural simulations using the pore morphology method (MSS).[19]

$$p_c(s_l) = p_d(1 - s_l)^{-1/h} \quad [20]$$

Here, the entry pressure p_d is the capillary pressure required to displace the wetting phase from the largest pore of the medium. The empirical parameter h accounts for the pore size distribution of the medium. The expression due to Van Genuchten is given by

$$p_c(s_l) = p_d[(1 - s_l)^{-1/m} - 1]^{1-m} \quad [21]$$

Figure 2 shows the capillary pressure–saturation relations proposed by Leverett, Brooks-Corey, and Van Genuchten together with the dataset obtained by Becker et al.[19] from microstructural simulation (MSS). The Brooks-Corey and Van Genuchten parameters h and m used for plotting represent typical values for soil tests.[27] The entry pressure p_d has been estimated for the GDL. Figure 2 shows that the Leverett expression, which is widely used for the description of liquid water transport in the porous layers of fuel cells, shows the greatest deviation from the simulation data. This is mainly because, in contrast to the Brooks-Corey function and the Van Genuchten expression, the Leverett function has a zero entry pressure. The three empirical expressions were fitted to the simulation data within the range of saturation values $0 \leqslant s_l \leqslant 0.8$ by using the data analysis program Origin. The best agreement was found for the expression proposed by Van Genuchten (Eq. 21), which is hence used in Eq. 3. In Fig. 3, the fitted Van Genuchten expression is shown for three different contact angles. Table I shows the parameters p_d and m resulting from this fitting procedure. As can be seen from Table I, a change in the contact angle only results in a change of the entry pressure p_d while m remains constant. This is used in the Discussion of Extracted Parameters section to transform each value of p_d obtained by simulation into the corresponding contact angle.

Analogously, several empirical correlations for the relative permeability as well as an expression for the diffusivity were fitted to the microstructural simulation data. For the relative permeability, three expressions were found. The expression which is most often used is the one obtained by Wang[18]

$$k_{rel,l}(s_l) = s_l^{\chi} \quad [22]$$

with

$$\chi = 3$$

Mualem[28] derived two expressions from the capillary pressure expressions given by Brooks-Corey and Van Genuchten, respectively. The Brooks-Corey expression for the relative permeability of liquid water in a hydrophobic medium is given by Eq. 23

$$k_{rel,l}(s_l) = s_l^{\xi}[1 - (1 - s_l)^{(2+h)/h}] \quad [23]$$

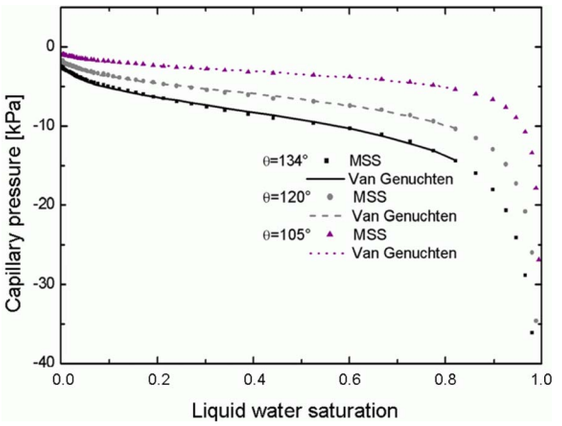

Figure 3. (Color online) Capillary pressure–saturation relation according to Van Genuchten, fitted to microstructural simulation data carried out by Ref. 19 using the pore morphology method (MSS) for three different contact angles. As shown in Table I, a change in the contact angle only leads to a change of the entry pressure p_d in Eq. 21 as a result of the fitting procedure, while m remains constant. Thus, each value of p_d obtained by modeling can be transformed into a corresponding contact angle using the microstructural simulation data.

The Van Genuchten expression is given by

$$k_{rel,l}(s_l) = s_l^{\gamma}[1 - (1 - s_l)^{1/m}]^{2m} \quad [24]$$

The best agreement with the simulation data was obtained for the Van Genuchten expression (Eq. 24), which is hence used in Eq. 1.

For the diffusivity of oxygen in Eq. 4, an expression obtained by Nam and Kavini,[4] who used a microscopic network model, was fitted to the microstructural simulation data. D_{O_2} is given by

$$D_{O_2} = D_{O_2}^0(1 - s_l)^{\delta}\pi\left(\frac{\pi - 0.11}{1 - 0.11}\right)^{d} \quad [25]$$

where $D_{O_2}^0$ is the vacuum diffusivity of oxygen, and the parameters are given by

$$\delta = 2.0$$

$$d = 0.79$$

Table II shows the two-phase parameters extracted for the Van Genuchten expressions for capillary pressure and relative permeability, as well as for the diffusivity obtained by Nam and Kaviany.

Simulation results.— In the following, the results for the liquid water saturation s_l and the volume fraction of oxygen y_{O_2} obtained by the model for a constant voltage $U_{sim} = 0.4$ V are depicted. In Table III, the base case parameters used for simulation are listed. A comparison between the simulation results in this section and the results obtained when using fitted model parameters is made in the Discussion of Extracted Parameters section. Figure 4 shows the time-dependent evolution of the liquid water saturation s_l for the GDL model. The x-axis corresponds to the one-dimensional GDL (see Fig. 1a), where a dimensionless distance of 0 is the boundary to the cathode $\partial\Omega_c$, and 1 is the boundary to the gas channels, $\partial\Omega_{ch}$. At $\partial\Omega_{ch}$ the saturation is set to zero. The initial value of the saturation is $s_l^0 = 0.01$. After approximately 3 s, s_l has reached its stationary value throughout the GDL. At $\partial\Omega_c$ the highest value of 0.06 is reached, because here the ORR takes place where water is produced. In Fig. 5, both the stationary saturation and the volume fraction of oxygen are shown for the model for the combination of GDL and MPL (see Fig. 1b). For this graph, scaled coordinates are used. The left boundary of the MPL is the boundary to the cathode, $\partial\Omega_c$. At the interface between MPL and GDL, the saturation exhibits a discontinuity which has already been modeled by Nam and Kaviany.[4] The discontinuity can be explained by the interface condition defined at this point, given by the continuity of the capillary pressure. Because the pore size distribution of the MPL is shifted to much smaller values compared to the GDL (which is accounted for by a lower intrinsic permeability $K_{int,MPL}$ in the simulation), according to the Young–Laplace equation

$$p_c = -\frac{2\sigma_l \cos\theta}{r} \quad [26]$$

the entry of a certain amount of liquid water into the medium requires a higher capillary pressure. Inversely, at a fixed capillary pressure value, the water saturation reaches a smaller value in the MPL than in the GDL, resulting in the discontinuity between both layers. The volume fraction of oxygen shows a linear behavior in both layers, starting from $y_{O_2} = 0.21$ at $\partial\Omega_{ch}$. The gradient of y_{O_2} in the MPL is higher than in the GDL. This is mainly due to the lower porosity of the MPL, which causes a lower diffusivity of oxygen according to Eq. 25.

Table I. Parameters resulting from fitting the capillary pressure–saturation relation of Van Genuchten to the microstructural simulation data obtained by Ref. 19 for three different contact angles.

	θ = 134°:	θ = 120°:	θ = 105°:
p_d (Pa)	-8.33×10^3	-6.0×10^3	-3.10×10^3
m	0.75	0.75	0.75

Table II. Two-phase parameters obtained by fitting the capillary pressure, relative permeability, and diffusivity expressions to microstructural simulation data obtained by Ref. 19.

Van Genuchten parameters for capillary pressure and relative permeability	
γ	1.85
m	0.75
p_d, Pa	-8.33×10^3 (θ = 134°)
Nam–Kaviani parameters for diffusivity	
d	1.1
δ	3.0

Table III. Base case parameters used in simulation results section.

Symbol	Value	Reference
Kinetic parameters		
aj_0, A/m^3	2×10^4	36 and 37
α	0.53	21
U_{sim}, V	0.4	—
T, K	313	—
Material parameters		
$K_{int,GDL}$, m^2	1.15×10^{-11}	MSS
$K_{int,MPL}$, m^2	1×10^{-12}	Est.
$p_{d,GDL}$, Pa	-8.33×10^3 (θ = 134°)	MSS
$p_{d,MPL}$, Pa	-10.0×10^3	Est.
π_{GDL}	0.5	37 and 38
π_{MPL}	0.4	37 and 38
Two-phase parameters		
β	1	Est.
γ	1.85	MSS
d	1.1	MSS
δ	3.0	MSS
m	0.75	MSS

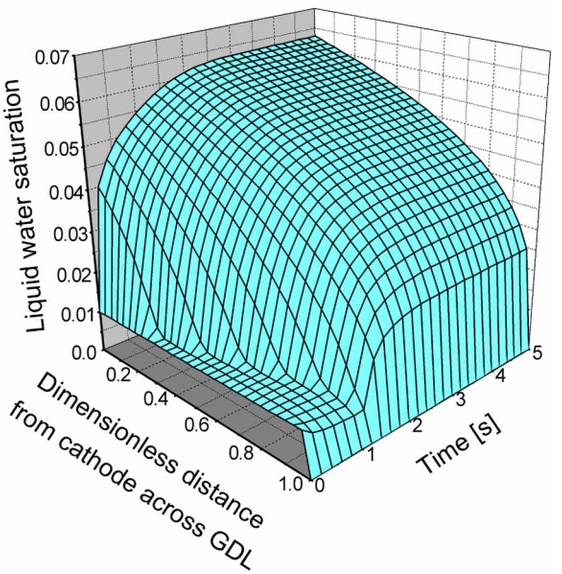

Figure 4. (Color online) Time evolution of the liquid water saturation in the GDL at a constant voltage of 0.4 V using the model parameters listed in Table III. The *x*-axis corresponds to the one-dimensional GDL model in Fig. 1a.

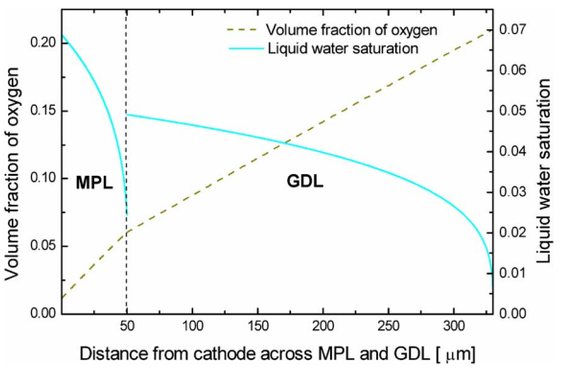

Figure 5. (Color online) Stationary liquid water saturation and volume fraction of oxygen in MPL and GDL. The model parameters used for the simulation are listed in Table III. The *x*-axis corresponds to the one-dimensional model in Fig. 1b using scaled coordinates. Due to the interface condition defined at the boundary $\partial\Omega_{in}$ between MPL and GDL, given by the continuity of the capillary pressure, and the lower pore size values in the MPL compared to the GDL, the saturation exhibits a discontinuity at $\partial\Omega_{in}$.

The time-dependent development of the saturation in the model for the combination of GDL and MPL (see Fig. 1b) is shown in Fig. 6. Figure 6a corresponds to the MPL where the boundary $\partial\Omega_c$ is located at a dimensionless distance of 0, and 1 is the boundary between MPL and GDL, $\partial\Omega_{in}$; Fig. 6b corresponds to the adjacent GDL. A comparison of both diagrams shows that the stationary value of the saturation is reached much faster in the MPL (after 1 s) than in the GDL, where it takes 5 s for the saturation to reach its equilibrium value. This can be explained by the different thickness values of both layers. The time required for an exponentially decaying process to reach $1/e$ of the initial value is given by the characteristic time constant τ_κ of layer κ

$$\tau_\kappa = \frac{d_\kappa^2}{D_{l,\kappa}^{eff}} \quad \text{with } \kappa = \text{GDL,MPL} \qquad [27]$$

where d_κ is the thickness of layer κ. As can be seen from Eq. 27, the greater thickness of the GDL causes a much higher time constant. Because of the different material properties, the effective diffusivity of water $D_{l,\kappa}^{eff}$ is also different for GDL and MPL, but compared to the thickness, the influence on the time constant can be neglected.

A comparison of Fig. 6b with Fig. 4 shows that the saturation in the GDL reaches a lower value ($s_l = 0.05$) when an MPL is inserted between the GDL and cathode than when the GDL is connected directly to the cathode ($s_l = 0.06$). This demonstrates the benefits of an inserted MPL, which can prevent the GDL from flooding. Here, the results of Nam and Kaviany[4] are reproduced, who concluded that the saturation step between the GDL and MPL leads to an improvement of the cell performance.

Model Validation

Fitting procedure.— The chronoamperometric measurements used for the validation of the model were carried out by Ziegler and Heilmann[20] at Fraunhofer Institute for Solar Energy. The potential step voltammetry and sine wave testing described by Ziegler and Heilmann were simulated using the GDL model (Fig. 1a). The voltage U_{sim} used for simulation was determined from the voltage U_{cell} applied to the test cell as described in the following. Ziegler and Heilmann used a reference cell setup that is depicted in Fig. 7. The voltage measured between anode and cathode is denoted U_{cell}. In each experiment, the voltage between the working cathode and the reference anode, U_{CRA}, was also measured. Because there is no load

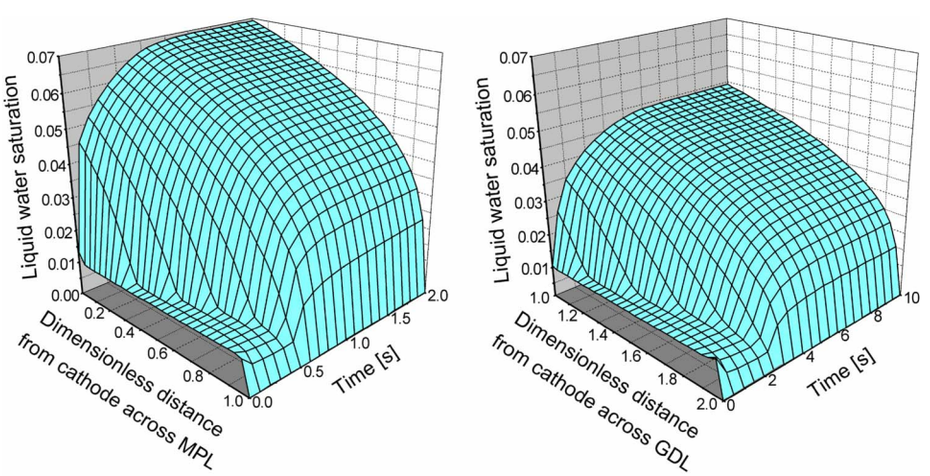

Figure 6. (Color online) Comparison of the time evolution of the liquid water saturation (a) in the MPL and (b) in the GDL. The model parameters used for the simulation are listed in Table III. The *x*-axis corresponds to the one-dimensional model in Fig. 1b. Due to the lower thickness of the MPL, the stationary value of the saturation is reached much faster in the MPL than in the GDL.

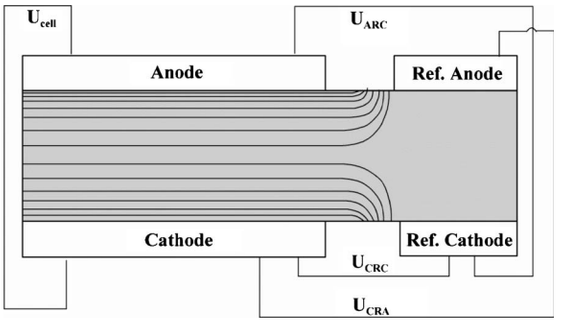

Figure 7. Experimental setup consisting of working and reference electrodes. In addition to U_{cell}, in each experiment the voltage between the working cathode and the reference anode, denoted U_{CRA}, was measured. From U_{CRA} and the measured 10 kHz impedance, an effective voltage U_{eff} was determined (Eq. 29) which is corrected for the anodic and the ohmic overpotentials that are not considered in the model. Further on, an analytical function was fitted to U_{eff}, yielding the voltage U_{sim} which was used for simulation.

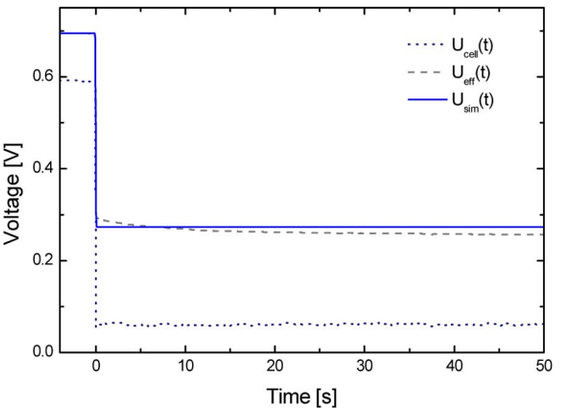

Figure 8. (Color online) Cell voltage $U_{cell}(t)$ measured by potential step voltammetry, corresponding effective voltage $U_{eff}(t)$, and voltage $U_{sim}(t)$ used for simulation. $U_{eff}(t)$ is corrected for the anodic and the ohmic overpotentials that are not considered in the model. U_{sim} is obtained by fitting a hyperbolic tangent U_{eff}.

on the reference anode, U_{CRA} does not contain the anode overpotential n_a. Furthermore, U_{CRA} contains only half of the ohmic membrane resistance if one assumes a symmetric potential distribution between anode and cathode, as shown in Fig. 7 by the potential lines. The sum of the ohmic membrane and contact resistances of the test cell, referred to as R_{ohm}, is given by the measured 10 kHz impedance. Assuming that the contact resistance is small compared to the membrane resistance, U_{CRA} can be written as a function of the measured current density j_m as follows

$$U_{CRA} = U_{cell} + \frac{1}{2}|j_m R_{ohm}| + |\eta_a| \quad [28]$$

From Eq. 28, an effective voltage U_{eff} can be calculated that is corrected for the anode and the ohmic overpotentials. U_{eff} is given by

$$U_{eff} = U_{CRA} + \frac{1}{2}|j_m R_{ohm}| \quad [29]$$

For each experiment, U_{eff} was calculated according to Eq. 29, then an analytical function was fitted to U_{eff}, yielding the voltage U_{sim} which was used for simulation.

By using the Nelder–Mead algorithm, the simulated current curves were fitted to their corresponding measured curves, where the same set of initial parameters was used in each case. The following function was minimized by the algorithm

$$f(\mathbf{a}) = \sum_{i=1}^{m} [j_c(\mathbf{a}, t_i) - j_m(t_i)]^2 \quad [30]$$

where $\mathbf{a}$ is the vector of the parameters to be fitted. $j_c(\mathbf{a},t_i)$ and $j_m(t_i)$ are the simulated and the measured current density at the discrete time value t_i, respectively. To calculate the function $f(\mathbf{a})$, the simulation values at t_i with $i = 1,2, \ldots ,m$ had to be extracted from the solution. The Nelder–Mead algorithm used to find the minimum of $f(\mathbf{a})$ is based on the simplex method. For N parameters to be optimized, $N+1$ initial parameter vectors $\mathbf{a}_1, \ldots ,\mathbf{a}_{N+1} \in \mathbb{R}^N$ are needed to form the corners of an N-dimensional simplex in the parameter space. The parameter vectors are varied such that the simplex moves in the direction of the optimum parameter vector and finally contracts with regard to this point. The termination criterion is defined by the diameter of the simplex and was set to 1×10^{-4}. The Nelder–Mead algorithm is implemented in the function *fminsearch* in the program Matlab, where it can be used to find the minimum of an analytical function. To apply *fminsearch* to the Comsol model of the GDL, both the model and the calculation of $f(\mathbf{a})$ according to Eq. 30 were implemented in Comsol Script. By defining the Comsol Script file as a Matlab function, *fminsearch* could then be used to fit the simulation to the experimental data.

Potential step voltammetry.— In this experiment, a voltage of 0.59 V was applied to the test cell while the impedance at 10 kHz was measured. As soon as the impedance remained constant, a voltage step from 0.59 to 0.06 V was imposed. The current response of the cell was sampled every 0.2 s for 50 s. The cell voltage can be expressed by

$$U_{cell}(t) = \begin{cases} U_{cell,1} : t < t_0 \\ U_{cell,2} : t \geq t_0 \end{cases} \quad [31]$$

with

$$U_{cell,1} = 0.59 \text{ V}$$

$$U_{cell,2} = 0.06 \text{ V}$$

The measured 10 kHz impedance R_{ohm} (see Ref. 20 for numerical data) and voltage U_{CRA} were used to calculate the effective voltage U_{eff} according to Eq. 29. U_{eff} and U_{cell} are shown in Fig. 8. Note that U_{eff} is higher than U_{cell} by the modulus of the anode and the ohmic overpotential. A hyperbolic tangent was fitted to U_{eff} and is given by

$$U_{sim}(t) = \frac{U_{sim,1} - U_{sim,2}}{e^{l(t-t_0)} + 1} + U_{sim,2} \quad [32]$$

with

$$U_{sim,1} = 0.70 \text{ V}$$

$$U_{sim,2} = 0.27 \text{ V}$$

$$l = 600 \text{ s}^{-1}$$

Considering that l must be high enough to ensure the steplike behavior of U_{sim}, but at the same time low enough to allow good convergence of the simulation, the value $l = 600 \text{ s}^{-1}$ was used. Together with the cell voltage U_{cell} and the effective voltage U_{eff}, U_{sim} is shown in Fig. 8. U_{sim} according to Eq. 32 was used to simulate the potential step voltammetry. The initial saturation was set to $s_1^0 = 0.56$. The Nelder–Mead algorithm was applied for $t \leq t_0$ and $(t_0 + t_1) \leq t \leq (t_0 + t_2)$, using $t_1 = 0.7$ s and $t_2 = 40$ s, to the simulated current density curve. Between t_0 and $t_0 + 0.7$ s the curve was not fitted, because the processes occurring during this period are not considered in the model. The discharge of the double-layer capacity takes place within 10^{-6} s. Processes in the active layer of the cath-

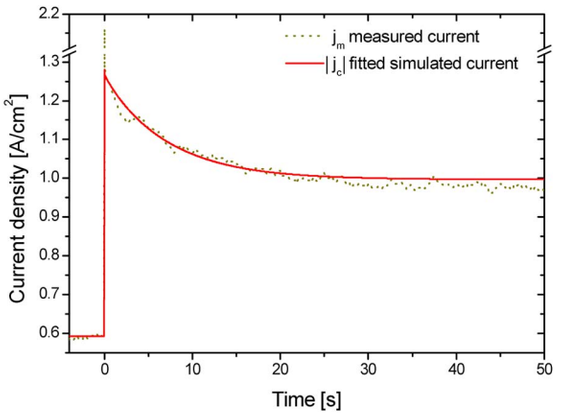

Figure 9. (Color online) Comparison of measured current density and fitted simulated current density for potential step voltammetry. The simulated current density refers to the boundary $\partial\Omega_c$ between GDL and cathode (Fig. 1a).

ode, like the diffusion of oxygen, occur within 10^{-3} s up to 1 s. Figure 9 shows a comparison of the fitted and the measured current density, given by j_c and j_m, respectively, where the time evolution of j_c refers to the boundary $\partial\Omega_c$ between the GDL and cathode. Simulation results and experimental data show very good agreement. The voltage step causes an instantaneous increase of the measured current density j_m from 0.6 to 2.1 A/cm^2. The ensuing decrease of j_m within 26 s to the value 1.0 A/cm^2 is due to the flooding of the pores and the resulting mass-transport limitation. Figure 10 shows the evolution of the liquid water saturation and the volume fraction of oxygen after the voltage step. Note that the change of the saturation by $\Delta s_l = 0.06$ is small compared to the considerable change of the simulated current density by $\Delta j_c = 0.27$ A (see Fig. 9). Figure 10 shows that the saturation reaches the value 0.485 when the simulation parameters are used that have been optimized by the Nelder–Mead algorithm. Compared to Fig. 4, where literature values have been used for the simulation parameters and the maximum saturation is 0.06, this is a much higher value. The volume fraction of oxygen decreases by $\Delta y_{O_2} = 0.10$. The opposite development of saturation and volume fraction of oxygen is due to the coupling between s_l and the diffusivity of oxygen D_{O_2} as well as the converse coupling of s_l and y_{O_2} to the current density via boundary conditions. A discussion of the parameters that have been extracted by the

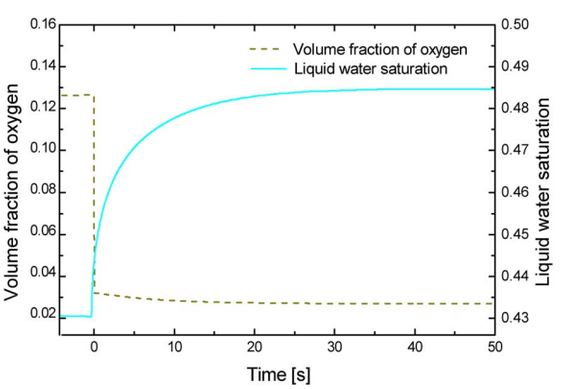

Figure 10. (Color online) Time evolution of liquid water saturation and volume fraction of oxygen at the boundary $\partial\Omega_c$ between GDL and cathode (Fig. 1a) for the simulated potential step voltammetry. The opposite development of saturation and volume fraction of oxygen is due to the coupling between s_l and the diffusivity of oxygen D_{O_2} as well as to the converse coupling of s_l and y_{O_2} to the current density via boundary conditions.

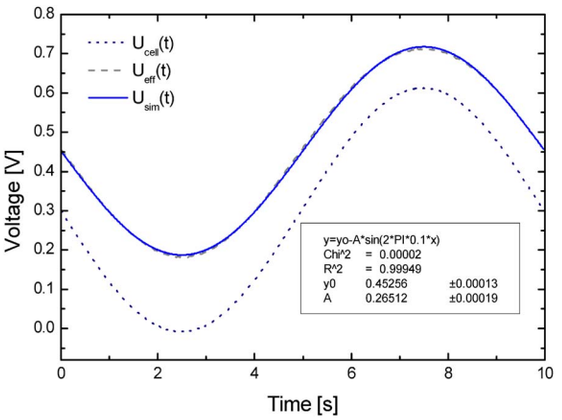

Figure 11. (Color online) Cell voltage $U_{cell}(t)$ measured by sine wave testing, corresponding effective voltage $U_{eff}(t)$, and voltage $U_{sim}(t)$ used for simulation. $U_{eff}(t)$ is corrected for the anodic and the ohmic overpotentials that are not considered in the model. U_{sim} is obtained by fitting a hyperbolic tangent to U_{eff}.

fitting algorithm is presented in the Discussion of Extracted Parameters section.

Sine wave testing.— A voltage of $U_{cell,0} = 0.3$ V was applied to the test cell. As soon as the measured impedance at 10 kHz remained constant, the direct voltage was superposed by an alternating voltage of amplitude $\Delta U_{cell} = 0.3$ V and frequency $f = 0.1$ Hz. The responding current density was sampled every 0.2 s. The voltage function applied to the test cell is given by

$$U_{cell}(t) = U_{cell,0} - \Delta U_{cell} \sin(2\pi f t) \quad [33]$$

with

$$U_{cell,0} = 0.3 \text{ V}$$

$$\Delta U_{cell} = 0.3 \text{ V}$$

$$f = 0.1 \text{ Hz}$$

The measured 10 kHz impedance R_{ohm} (see Ref. 20 for numerical data) and voltage U_{CRA} were used to calculate the effective voltage U_{eff} according to Eq. 29. A sine wave was fitted to U_{eff} and is given by

$$U_{sim} = U_{sim,0} - \Delta U_{sim} \sin(2\pi f t) \quad [34]$$

where

$$U_{sim,0} = 0.45 \text{ V}$$

$$\Delta U_{sim} = 0.27 \text{ V}$$

Figure 11 shows U_{sim} together with the effective voltage U_{eff} and the cell voltage U_{cell}. U_{sim} according to Eq. 34 was used to simulate the sine wave testing. The initial saturation was set to $s_l^0 = 0.50$. The Nelder–Mead algorithm was applied to a single oscillation. Figure 12 shows the fitted and the measured current density, given by j_c and j_m, respectively, where the time evolution of j_c refers to the boundary $\partial\Omega_c$ between the GDL and cathode. The simulated and the measured curves for the current density agree very well. The current density oscillates conversely to the voltage with a phase shift of $\varphi_1 = -12.6°$ between the minimum voltage and the maximum measured current density j_m. Because the major physical process corresponding to low frequencies is the transport of liquid water through the porous GDL, the phase shift can be explained by the flooding of the pores and the resulting mass-transport limitation. Even before the minimum voltage is reached, the fraction of water-filled pores is high enough to hinder the gas from reaching the electrode, which

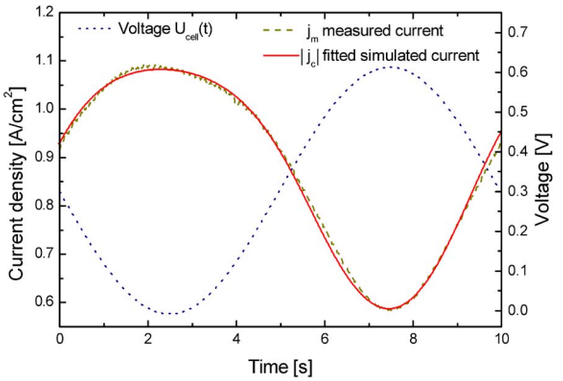

Figure 12. (Color online) Comparison of measured current density and fitted simulated current density for the sine wave testing. The simulated current density is referred to the boundary $\partial\Omega_c$ between GDL and cathode (Fig. 1a).

results in a flattening of the upper part and finally in a decrease of the current density curve. With $\varphi = -9°$ in the simulation, the phase shift between voltage and simulated current density j_c is reproduced sufficiently.

Figure 13 shows the simulated water saturation and the volume fraction of oxygen. Within one oscillation, the change of the saturation by just $\Delta s_l = 0.02$ is accompanied by a significant change of the oxygen volume fraction. The opposite oscillation of s_l and y_{O_2} is due to the two-phase coupling of both quantities as well as to their converse coupling to the current density via boundary conditions.

Discussion of Extracted Parameters

In Table IV the initial parameters used for the potential step voltammetry (PSV) and sine wave testing (SWT) simulations are listed. The nine parameters that were optimized by the Nelder–Mead algorithm are marked with stars; the remaining parameters were set to fixed values and kept constant. The fitted parameters are very close to the initial values. Due to the dependence of the fitted parameters on the initial values, a well-founded choice of the latter has to be made. Table IV shows that the fitted parameters are also close to each other (the maximum deviation is 19% for the two-phase parameter β). This means that the model predicts the current behavior for the two experiments accurately while using almost the same set of parameters.

Table IV also compares the model parameters to their corresponding literature values as far as they have been reported. The

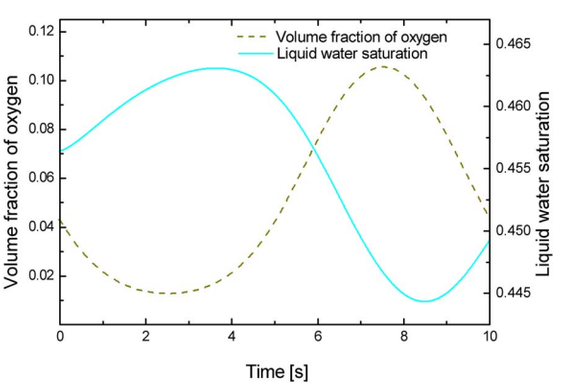

Figure 13. (Color online) Time evolution of liquid water saturation and volume fraction of oxygen at the boundary $\partial\Omega_c$ between GDL and cathode (Fig. 1a) for the simulated sine wave testing. The change of the saturation by just $\Delta s_w = 0.02$ is accompanied by a significant change of the oxygen volume fraction.

Table IV. Comparison of initial and fitted parameters for potential step voltammetry and sine wave testing.

		Fitted values			
Symbol	Initial value	PSV	SWT	Lit.	value
Kinetic parameters					
aj_0^*, A/m³	1.9×10^9	1.6×10^9	1.9×10^9	—	
α	0.14	—	—	0.53	[29]
T(PSV), K	313	—	—	—	
T(SWT), K	315	—	—	—	
Material parameters					
$K^*_{int,GDL}$, m²	1.2×10^{-11}	1.2×10^{-11}	1.2×10^{-11}	—	
$p^*_{d,GDL}$, Pa	−1.1	−0.99	−1.10	—	
π^{GDL}_*	0.5	0.51	0.50	0.78	(TDG)
θ_{GDL}, °	90.005	90.005	90.005	134	(TDG)
Two-phase transport parameters					
β*	0.5	0.62	0.50	—	
γ*	1.85	1.82	1.86	0.33	[27]
d*	0.6	0.55	0.61	0.79	[4]
δ*	3.4	3.34	3.42	2	[4]
m*	0.75	0.76	0.75	0.77	[27]

kinetic parameters of the ORR have been experimentally studied in Ref. 29-35. While well-recognized values for α can be obtained from the literature, it is difficult to get consistent values for aj_0. Therefore, only α is compared to its literature value. As can be seen from Table IV, there is a significant deviation between the value used for simulation (α = 0.14) and the literature value (α = 0.53[29]). The choice of α to 0.14 can be explained by the following estimate using the Tafel equation. The absolute value of the current density, $|j_c|$, is given by

$$|j_c| = C \times \exp\left[\frac{-\alpha F}{RT}(U_{sim} - U_{oc})\right] \quad [35]$$

where the factor C is given by

$$C = (1 - s_l)^{\beta} d_c a j_0 y_{O_2} \quad [36]$$

Plotting $|j_c|$ against the voltage U_{sim}, it appears that the slope of the curve increases rapidly with increasing α. This is shown in Fig. 14 for three different values of α. The two points $P_1^\star$ and $P_2^\star$ marked in the diagram, where $P_1^\star$ is given by $U_{sim} = 0.30$ V, $j_c = 1.01$ A/cm², and $P_2^\star$ is given by $U_{sim} = 0.60$ V, $j_c = 0.78$ A/cm², correspond to measuring points in the sine wave testing at 0.1 Hz (Fig. 12). These

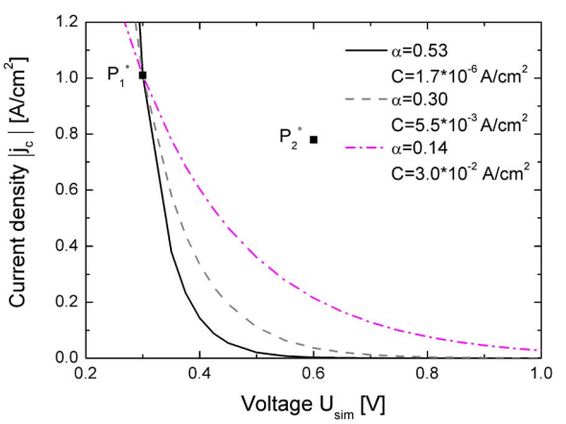

Figure 14. (Color online) Current density $|j_c|$ according to Eq. 35 for different values of α. The factor C is adjusted for each curve such that all curves intersect in the point P_1^* which corresponds to a measuring point in the sine wave testing (P_1 in Fig. 15). For α = 0.14 the model predicts the measured behavior of the current density.

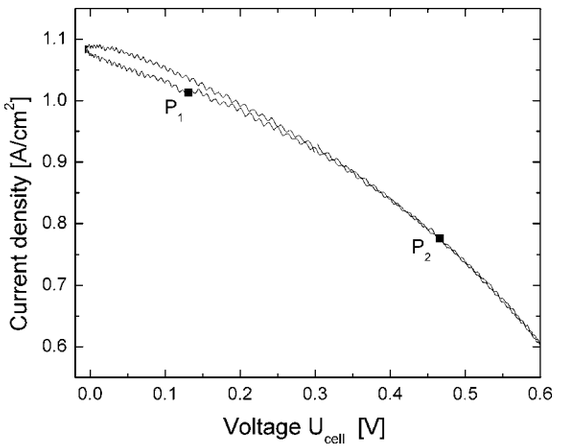

Figure 15. Measured current density for the sine wave testing, plotted vs the cell voltage U_{cell}. The measuring points P_1 and P_2 correspond to P_1^* and P_2^* in Fig. 14.

measuring points, denoted as P_1 and P_2, are shown in Fig. 15, where the measured current density is plotted against the cell voltage U_{cell} for the sine wave testing. P_1 is given by $U_{cell} = 0.13$ V, $j_c = 1.01$ A/cm^2, and P_2 is given by $U_{cell} = 0.47$ V, $j_c = 0.78$ A/cm^2. $P_1^\star$ and $P_2^\star$ in Fig. 14 are derived from P_1 and P_2 by replacing the measured voltage U_{cell} with the corresponding voltage U_{sim}, which can be done by plotting $U_{sim}(t)$ (Eq. 33) and $U_{cell}(t)$ (Eq. 34) against each other as shown in Fig. 16. In Fig. 14 the factor C is adjusted for each curve such that all curves coincide at the point $P_1^\star$. To predict the measured behavior, the simulated current density curve has to touch this point. If the literature value $\alpha = 0.53$ is used, $|j_c|$ exhibits a steep increase from higher to lower voltages. Accordingly, C has to be chosen sufficiently low to put the curve through $P_1^\star$. However, this results in current density values too low for voltages higher than $U_{sim} = 0.6$ V (2.9×10^{-3} A/cm^2 at 0.6 V). Although y_{O_2} and the term $(1 - s_l)^\beta$ increase with increasing voltage due to the mass-transport limitation, and so does the factor C according to Eq. 36, to put the curve through $P_2^\star$, C would have to be approximately 350 times higher than in $P_1^\star$ which cannot be achieved by varying y_{O_2} and s_l. Hence, for $\alpha = 0.53$, the model does not predict the measured behavior of the current density. For $\alpha = 0.3$, the simulated current

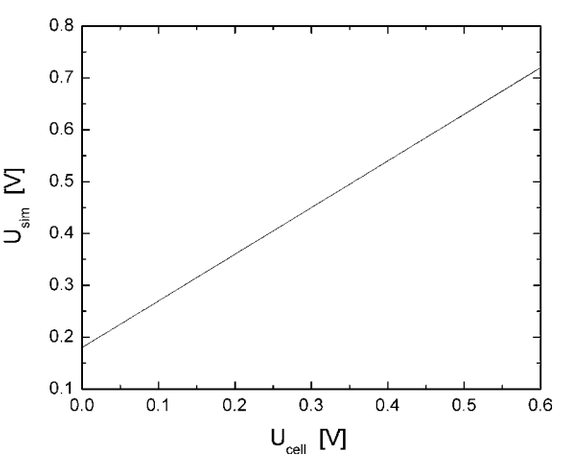

Figure 16. Plot of $U_{sim}(t)$ vs $U_{cell}(t)$ according to Eq. 33 and 34 for the sine wave testing. Using the plot, values of U_{cell} can be converted directly into values of U_{sim}.

density is still too low at 0.6 V (3.7×10^{-2} A/cm^2); C would have to be increased more than 20 times in $P_2^\star$ compared to $P_1^\star$. The optimum value for α turned out to be 0.14. At 0.6 V, $|j_c|$ reaches 0.21 A/cm^2. To put the curve through $P_2^\star$, C has to be increased by the factor 3.7. This is reflected by the model description of the mass-transport limitation. The optimized value of aj_0, which is on the order of 10^9 A/m^3 for both simulations, can be explained with regard to the above. For $\alpha = 0.14$, C has to be set to 3.0×10^{-2} A/cm^2, that is 3.0×10^2 A/m^2, to put the curve through $P_1^\star$. Estimating that y_{O_2} is on the order of 10^{-1} at $U_{sim} = 0.6$ V, and the term $(1 - s_l)^\beta$ is on the order of 1, according to Eq. 36, aj_0 has to be on the order of 10^8 to 10^9 A/m^3. Summarizing the above, the simplifying description of the current density by the Tafel equation results in the specific choice of the kinetic parameters. For example, the complex flooding process in the cathode is not considered sufficiently in the model. An additional term accounting for this process might constrain the exponential slope in Eq. 35 and allow for the choice of $\alpha > 0.14$.

The optimized material parameters in Table IV, except for the intrinsic permeability $K_{int,GDL}$, are compared with the corresponding values given by the manufacturer of the Toray GDL, Toray Deutschland GmbH (TDG). For the determination of $K_{int,GDL}$ to 1.2×10^{-11} m^2, the relation $K_{int,GDL} = k_{rel,l}(s_l = 1)$ was used, where $k_{rel,l}$ was obtained by fitting the Van Genuchten expression (Eq. 24) to the microstructural simulation results of Becker et al.[19]. For the porosity π_{GDL} of the Toray GDL, the manufacturer states 0.78, but in order to account for the decrease of the porosity due to the compression of the GDL, 0.5 was assumed in the model. From each entry pressure $p_{d,GDL}$ used in the simulation, the correlated contact angle θ_{GDL} was determined by using the microstructural simulation data in Ref. 19. In the following, the optimized contact angle is rounded off to the value 90.01° for the simulations. Here, a significant deviation from the value stated by the manufacturer, 134°, appears; the optimized contact angle corresponds to a much less hydrophobic GDL. Note that θ_{GDL} reflects the average contact angle of the GDL in the model, while in reality, the GDL is subject to local fluctuations of the wettability. The choice of the initial value for p_d can be explained as follows. The liquid water saturation increases by decreasing p_d and accordingly by decreasing θ_{GDL}. As can be seen from the diffusivity of oxygen D_{O_2} (Eq. 25), the water saturation level controls the two-phase coupling of water and oxygen via the term $(1 - s_l)^\delta$. If an entry pressure of 8.3 kPa is used in the simulation, corresponding to a contact angle of 134°, the maximum saturation at a cell voltage of 0.4 V reached in the GDL geometry is 0.06 (Fig. 4). This value is too low to allow significant influence of the term $(1 - s_l)^\delta$ on the simulation result. To make fine adjustment of the curve possible, the saturation level needs to be higher. An entry pressure between -1 and -1.2 Pa (corresponding to a contact angle of approximately 90.01°), yielding a saturation of maximally 0.5 at 0.4 V in the GDL model, led to the best possible fit of the simulated to the measured curve.

In the modeling and simulation section, a first set of two-phase parameters was extracted by comparing literature expressions of capillary pressure, relative permeability, and diffusivity of oxygen to the microstructural simulation results obtained by Ref. 19 et al. The initial values for the two-phase parameters needed for the application of the Nelder–Mead algorithm were chosen close to these first values. In Table IV, the optimized values of the two-phase parameters are compared to their corresponding literature values. The significant deviation of γ from the literature value in Ref. 27 is due to the differing application of the according Van Genuchten expression (Eq. 24), which is in Ref. 27 used to describe soil tests.

Figure 17 shows the time-dependent water saturation in the GDL model (Fig. 1a) at a cell voltage of 0.4 V, where the parameters extracted for the potential step voltammetry have been used for simulation. A comparison to Fig. 4, where the base case parameters according to Table III have been used for simulation, reveals two characteristics. First, the saturation reaches much higher values

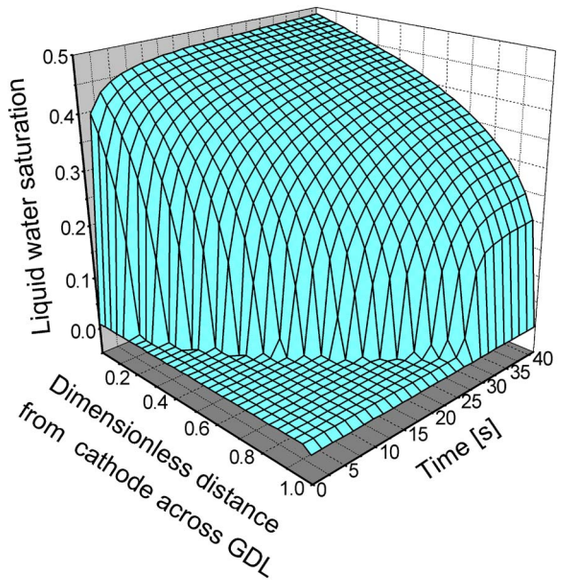

Figure 17. (Color online) Time evolution of the liquid water saturation in the GDL at a constant voltage of 0.4 V using fitted model parameters (Table IV). The *x*-axis corresponds to the one-dimensional model in Fig. 1a.

in Fig. 17; the maximum saturation is $s_l = 0.48$ compared to $s_l = 0.06$ in Fig. 4. This difference is mainly due to the lower contact angle of 90.01°. Second, the time constant is much higher in Fig. 17: Reaching a stationary value takes 30 s for s_l, while in Fig. 4 the equilibrium value is reached after just 3 s. This can be explained by the effective diffusivity of water $D_{l,eff}$ in the GDL derived from Eq. 1. $D_{l,eff}$ is given by

$$D_{l,eff} = \frac{1}{\mu_l \tau_{GDL}} k_{rel,l} K_{int,GDL} \frac{\partial p_l}{\partial s_l} \quad [37]$$

A decrease of the entry pressure $p_{d,GDL}$ corresponding to a decrease of the contact angle θ_{GDL} lowers the capillary pressure p_c (Eq. 21), and hence the term $\partial p_l / \partial s_l$ in Eq. 37. To a minor degree, the two-phase parameters contained in the relative permeability of water $k_{rel,l}(s_l)$ (Eq. 24) and in p_c have an influence on the effective diffusivity of water.

Conclusion

A one-dimensional dynamic two-phase model for the GDL was developed. Important saturation-dependent parametrizations were determined by comparing several literature parametrizations to the results of microstructural simulation data obtained by Becker et al.[19] Capillary pressure and relative permeability are described by Van Genuchten expressions, and the diffusivity of oxygen is described by an expression of Nam and Kaviany. The model was used to simulate two chronoamperometric experiments, potential step voltammetry, and sine wave testing at 0.1 Hz. A comparison between simulation and measurement data was made by using the fitting algorithm of Nelder and Mead. The model predicts the measured time-dependent current behavior for both experiments accurately, and hence describes the mass-transport limitation due to the dynamic flooding of the pores with liquid water adequately for these experiments. As a result of the optimization, important material and two-phase parameters have been extracted. In particular, the extracted contact angle indicates a less hydrophobic interior of the GDL than usually assumed. The method used to fit simulation results to dynamic experimental data is useful for further quantitative comparisons between two-phase models and experiments.

Fraunhofer Institute for Solar Energy Systems assisted in meeting the publication costs of this article.

List of Symbols

aj_0	exchange current density × active area of cathode, A/m^3
d	Nam–Kaviani parameter
d_c	thickness of cathode, 10 μm
d_{GDL}	thickness of GDL, 280 μm
d_{MPL}	thickness of MPL, 50 μm
D_{O_2}	diffusivity of oxygen, m^2/s
$D^0_{O_2}$	vacuum diffusivity of oxygen, 1.8×10^{-5} m^2/s
F	Faraday constant, 9.6485×10^4 C/mol
f	sine wave testing frequency, Hz
$j_{c/m}$	simulated/measured current density, A/m^2
$K_{int,GDL/MPL}$	intrinsic permeability of GDL/MPL, m^2
$k_{rel,l}$	relative permeability of water
m	Van Genuchten parameter
M_l	molar mass of water, 0.018 kg/mol
M_{O_2}	molar mass of oxygen, 0.032 kg/mol
p_l	liquid water pressure, Pa
p_g	gas pressure, Pa
p_d	entry pressure, Pa
p_c	capillary pressure, Pa
R	universal gas constant, 8.314 J/(kg mol)
R_{ohm}	ohmic resistance of test cell, Ω m^2
s_l	liquid water saturation
T	temperature, K
U_{cell}	voltage of test cell, V
U_{eff}	effective voltage, V
U_{oc}	open-circuit voltage of test cell, 0.98 V
U_{sim}	simulated voltage, V
y_{O_2}	volume fraction of oxygen
z	number of electrons involved in ORR, 1

Greek

α	asymmetry factor
β	parameter for coupling current density and saturation
γ	Van Genuchten parameter
δ	Nam–Kaviani parameter
η_c	cathode overpotential, V
θ_{GDL}	contact angle of GDL, °
μ_l	viscosity of liquid water, Pa s
π_{GDL}	porosity of GDL
π_{MPL}	porosity of MPL
ρ_l	mass density of liquid water, kg/m^3
ρ_{O_2}	mass density of oxygen, kg/m^3

References

1. C.-Y. Wang, *Chem. Rev. (Washington, D.C.)*, **104**, 4727 (2004).
2. U. Pasaogullari and C.-Y. Wang, *J. Electrochem. Soc.*, **151**, A399 (2004).
3. U. Pasaogullari and C.-Y. Wang, *Electrochim. Acta*, **49**, 4359 (2004).
4. J. Nam and M. Kaviany, *Int. J. Heat Mass Transfer*, **46**, 4595 (2003).
5. Z. H. Wang, C. Y. Wang, and K. S. Chen, *J. Power Sources*, **94**, 40 (2001).
6. E. Birgersson, M. Noponen, and M. Vynnycky, *J. Electrochem. Soc.*, **152**, A1021 (2005).
7. T. V. Nguyen and D. Natarajan, *J. Electrochem. Soc.*, **148**, A1324 (2001).
8. L. You and H. Liu, *Int. J. Heat Mass Transfer*, **45**, 2277 (2002).
9. M. Hu, A. Gu, M. Wang, X. Zhu, and L. Yu, *Energy Convers. Manage.*, **45**, 1861 (2004).
10. H. Sun, H. Liu, and L.-J. Guo, *J. Power Sources*, **143**, 125 (2005).
11. R. M. Rao, D. Bhattacharyya, R. Rengaswamy, and S. R. Choudhury, *J. Power Sources*, **173**, 375 (2007).
12. M. Acosta, C. Merten, G. Eigenberger, H. Class, R. Helmig, B. Thoben, and H. Müller-Steinhagen, *J. Power Sources*, **159**, 1123 (2006).
13. C. Ziegler, H. M. Yu, and J. O. Schumacher, *J. Electrochem. Soc.*, **152**, A1555 (2005).
14. D. Song, Q. Wang, Z.-S. Liu, and C. Huang, *J. Power Sources*, **159**, 928 (2006).
15. H. Meng, *J. Power Sources*, **171**, 738 (2007).
16. Y. Wang and C.-Y. Wang, *J. Electrochem. Soc.*, **154**, B636 (2007).
17. K. S. Udell, *Int. J. Heat Mass Transfer*, **28**, 485 (1985).
18. C. Wang and P. Cheng, *Int. J. Heat Mass Transfer*, **39**, 3607 (1996).
19. J. Becker, V. Schulz, and A. Wiegmann, *J. Fuel Cell Sci. Technol.*, **5**, 021006 (2008).
20. C. Ziegler and T. Heilmann, *J. Electrochem. Soc.*, **155**, B349 (2008).
21. C. Song, Y. Tang, J. L. Zhang, J. Zhang, H. Wang, J. Shen, S. McDermid, J. Li, and P. Kozak, *Electrochim. Acta*, **52**, 2552 (2007).
22. D. Gerteisen, A. Hakenjos, and J. O. Schumacher, *J. Power Sources*, **173**, 346 (2007).
23. J. Ihonen, F. Jaouen, G. Lindbergh, A. Lundblad, and G. Sundholm, *J. Electrochem. Soc.*, **149**, A448 (2002).
24. A. Parthasarathy, B. Dave, S. Srinivasan, and A. J. Appleby, *J. Electrochem. Soc.*, **139**, 1634 (1992).
25. R. J. Brooks and A. T. Corey, "Hydraulic properties of porous media," *Hydraulic Paper 3*, Colorado State University, Fort Collins, CO (1964).

26. M. T. van Genuchten, *Soil Sci. Soc. Am. J.*, **44**, 892 (1980).
27. R. Helmig, *Multiphase Flow and Transport Processes in the Subsurface*, Springer, Heidelberg (1997).
28. Y. Mualem, *Water Resour. Res.*, **12**, 513 (1976).
29. A. Parthasarathy, S. Srinivasan, A. J. Appleby, and C. R. Martin, *J. Electrochem. Soc.*, **139**, 2530 (1992).
30. A. Parthasarathy, C. R. Martin, and S. Srinivasan, *J. Electrochem. Soc.*, **138**, 916 (1991).
31. O. Antoine, Y. Butel, and R. Durand, *J. Electroanal. Chem.*, **499**, 85 (2001).
32. S. Mukerjee, S. Srinivasan, and A. J. Appleby, *Electrochim. Acta*, **38**, 1661 (1993).
33. A. Parthasarathy, S. Srinivasan, and A. J. Appleby, *J. Electroanal. Chem.*, **339**, 101 (1992).
34. A. J. Appleby, *J. Electroanal. Chem.*, **24**, 97 (1970).
35. A. Damjanovic, *J. Electroanal. Chem.*, **355**, 57 (1993).
36. H. Ju, G. Luo, and C.-Y. Wang, *J. Electrochem. Soc.*, **154**, B218 (2007).
37. U. Pasaogullari and C.-Y. Wang, *J. Electrochem. Soc.*, **152**, A380 (2005).
38. C. H. Min, Y. L. He, X. L. Liu, B. H. Yin, W. Jiang, and W. Q. Tao, *J. Power Sources*, **128**, 173 (2004).